RSC Advances

ROYAL SOCIETY OF CHEMISTRY

www.rsc.org/advances

A table of contents entry

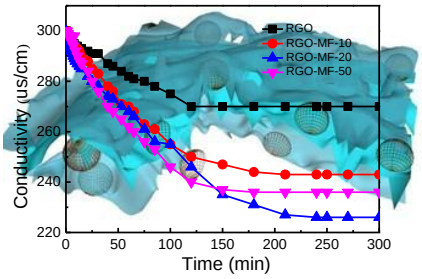

Nitrogen-doped graphene composites were prepared by incorporating melamine formaldehyde nanoparticles as high performance electrodes for capacitive deionization.

Journal Name

RSCPublishing

ARTICLE

Nitrogen-doped graphene composites as efficient electrodes with enhanced capacitive deionization performance

Xiaoyu Gu, Yu Yang, Yang Hu, Meng Hu, Jian Huang and Chaoyang Wang*

Cite this: DOI: 10.1039/xoxxooooox

Received ooth January 2012,
Accepted ooth January 2012

DOI: 10.1039/xoxxooooox

www.rsc.org/

Desalination of seawater and brackish water is a desirable technique to address actual water scarcity today and in the uncertain future. Three-dimensional reduced graphene oxide-melamine formaldehyde composites (3D RGO-MF) are prepared by carbonization of GO-MF composites which are prepared through the electrostatic attraction between GO and MF nanoparticles. The obtained composites exhibit a hierarchical porous structure with a specific surface area of 352 m^2/g and abundant nitrogen doping of 10.86%. Thus, they have an enhanced specific capacity of 76.8 F/g, which is much larger than that of pristine RGO electrode (23 F/g). With the enhanced electrochemical capacity, the as-prepared nitrogen-doped grephene composite are successfully employed as high performance electrodes for capacitive deionization. The excellent electrochemical capacity with low inner resistance and high reversibility endows the 3D RGO-MF electrodes with outstanding specific electrosorptive capacity of 21.93 mg/g at a direct voltage of 2.0 V in NaCl aqueous solution. It is confirmed that the 3D RGO-MF electrode is quite appropriate for high-performance capacitive deionization.

Introduction

Environmental problems, especially water crisis, have become more and more serious because of the rapid development of modern industry. Delivering safe potable water to human has been an impending challenge. However, most of the water on the earth is seawater or brackish water. Therefore, exploring energy efficient and cost-effective techniques for removal of salts from brackish water is meaningful and imperative. Until now, the most widely used processes for desalination are membrane separation and thermal separation. However, many shortcomings are still existed in these systems, such as energy consuming, low efficiency, and secondary pollution.[1, 2] Capacitive deionization (CDI) is an electrosorption process that involves application of an electric field between two electrodes to force ionic species toward oppositely charged electrodes,[3, 4] have attracted a wide interest in the adsorption processes for the treatment of wastewater and the purification of water supply.[5] At the water-electrode interface in CDI device, electrical double layers (EDLs) are formed and ions are electrosorbed in it. In relation to its working principle, the EDLs of the electrodes are directly dependent on the specific surface area and bulk conductivity, while the total surface is intrinsically determined by the pore size and shape.[6] In general, small pores and high total pore volumes lead to larger specific surface area (SSA).[7] Especially mesoporous structure (2-50 nm), guarantees not only a large accessible surface area for ion adsorption, but also a low-resistant pathway for ion transport through the framework. Furthermore, it has also been demonstrated that hierarchical porous materials containing interconnected macroporous, mesoporous and microporous structures have enhanced electrochemistry performance compared with single sized pore materials.[8] Therefore, compared with 2D packed materials, the 3D porous materials which consist of a high specific area and numerous porous channels for rapid ion and electron transport would be a desirable electrodes for CDI applications.

Taking advantage of the extended specific surface area, conductivity, and porous structure, carbon materials are ideal candidates for CDI application.[9] Hence, activated carbon,[10] carbon aerogels,[11, 12] mesoporous carbon,[13-15] carbon nanotubes and their composites,[16-21] have been widely subjected to extensive investigations by many research groups. In particular, graphene, a new carbon material with one-atom thickness and two-dimensional plane, has attracted considerable attention because of its excellent mechanical, electrical, photovoltaic, and optical properties.[22-26] However, due to the strong π-π interaction, the easy restacking takes place inside reduced graphene oxide (RGO) during preparation, which leads to a relatively low specific surface area and low bulk conductivity of as-prepared graphene, hampering its application in CDI.[27-29] Therefore, seeking proper materials to minimize the restacking effects, increase the conductivity in the vertical direction and

enhance the electrosorption performance of graphene has become a great challenge.[30, 31] In addition, among numerous methods proposed for tailoring or improving the physico-chemical properties of graphene, chemical doping is considered as an effective way to increase the density of charge-carrier and to enhance the electrical conductivities.[32-34] Nitrogen is considered as a potential element for the chemical doping because of its similar atom size and five valence electrons that can form valence bonds with carbon atoms.[35-38]

Herein, nitrogen doped carbon electrodes were synthesized by carbonization of graphene oxide-melamine-formaldehyde (GO-MF) composites which were prepared through the electrostatic attraction between GO sheets and MF nanoparticles. The detailed preparation process of 3D RGO-MF composites is shown in Fig. **1**. First, the dispersion of positively charged MF nanoparticles was mixed with negatively charged GO dispersion according to a certain ratio. Owing to the electrostatic interactions between GO sheets and MF nanoparticles, GO can be uniformly distributed in polymer matrix without aggregation and result in GO sheets directly and tightly contacting between them. After filtration and carbonization, 3D hierarchy porous RGO-MF composites are obtained with abundant N-doping. The as-prepared nitrogen-doped graphene composites as working electrodes show enhanced specific capacitance in electrochemical performance and outstanding specific electrosorptive capacity in CDI performance, indicating significant improvement for the 3D RGO-MF composites as compared to pristine RGO.

Experimental section

Materials

Natural graphite powder and polyvinyl alcohol were purchased from J&K Scientific Ltd. (China). Melamine was purchased from Sinopharm chemical reagent Co., Ltd. and acetylene black was purchased from Shanxi LZY battery material Co., Ltd (China). All other reagents were purchased from Guangzhou Chemical Reagent Co. (China) and used without further purification. Water used in all experiments was deionized and filtrated by a Millipore purification apparatus with resistivity more than 18.0 MΩ·cm.

Preparation of RGO-MF composites

Monodisperse MF nanoparticles with the diameter of about 280 nm were prepared according to our previously reported method,[39, 40] as shown in Fig. S1. The experimental procedure is described in Supporting Information. The as-prepared MF spheres were re-dispersed in water to obtain an aqueous dispersion (5 mg/mL) for further use. GO was prepared from purified natural graphite via the modified Hummer's method,[41] and the corresponding details could be found in our previous report.[42] A dispersion of GO sheets was obtained by ultrasonication for 2 h in water.

The obtained positively charged MF nanoparticles were assembled with negatively charged GO sheets by electrostatic interactions, resulting in a suspension. To assemble 3D interconnected RGO-MF composites, GO dispersion with different concentrations and MF nanoparticle dispersion were simultaneously added dropwise to an empty container under stirring to make the mass ratio of MF to GO, 10:1, 20:1, 50:1, 100:1, and 200:1. The as-prepared GO-MF flocculation was named as GO-MF-10, -20, -50, -100 and -200, respectively. Under the optimal assembly conditions, almost all the spheres were encapsulated and connected by GO in the complexes, leaving a transparent aqueous solution. Finally, the resulting precipitates were made into films by vacuum filtration and washing by water twice. The above GO-MF composites were air dried at room temperature overnight. The GO-MF composites were annealed at 700 ^{o}C for 7 h under N_2 atmosphere with a heating rate of 5 ^{o}C/min in a tubular furnace. GO within the composite was thermally reduced into graphene and MF nanoparticles were transferred into N-doped carbon

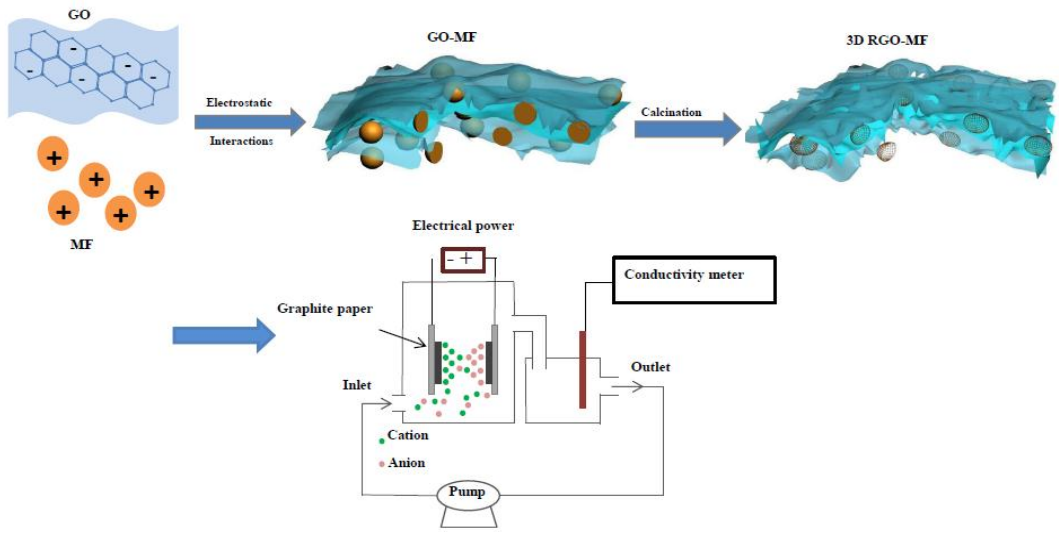

Fig. 1 Schematic illustration of the synthetic route for 3D RGO-MF electrodes as CDI applications

Journal Name RSCPublishing

ARTICLE

phase, so as to get the 3D RGO-MF composites. For comparison, traditional reduced graphene oxide (RGO) was prepared by a similar procedure, without MF nanoparticles incorporation.

Electrochemical measurements

The working electrode was prepared by pressing a paste of RGO-MF composite (80 wt%), acetylene black (10 wt%) and polytetrafluoroethylene (10 wt%) onto a nickel foam plate. Before casting and pressing, the raw mixture was ground for several hours to increase its homogeneity. The electrodes were dried at room temperature overnight before investigation of the electrochemical performance of the electrodes. A three-electrode cell system, including graphene-based electrode, Pt foil and Ag/AgCl (3 M KCl) were used as the working, counter and reference electrodes. All of the experiments were carried out in 0.5, 1 or 1.5 M NaCl aqueous electrolyte.

Cyclic voltammetry (CV) analysis of graphene-based electrodes was measured using an electrochemical workstation (CHI660C instruments, Shanghai, China). The potential range for CV was -1.0-0 V. The effects of changes in the scan rate were examined by supplying 0.01, 0.02 or 0.05 V/s and the concentration of NaCl solution was kept at the constant of 0.5 M.

The galvanostatic charge/discharge tests were conducted on an automatic LAND battery test instrument (CT2001A) to evaluate the charge-discharge performance in a 0.5 M NaCl aqueous solution. Here, the specific capacitances Cs were from the slope of discharge curves by using the following equation:

$$C_s = \frac{I\Delta t}{m\Delta V} \quad (1)$$

Where Cs (F/g) is the specific capacitance, I (A) is the constant discharge current, Δt (s) is the discharging time, m (g) is the mass of working electrode in milligram scale, ΔV is the voltage drop upon discharging (excluding the iR drop).

Electrochemical impedance spectroscopy (EIS) measurements were also measured by CHI 660C. The amplitude of the alternating voltage was 5 mV around the equilibrium potential (0 V) and the data was collected in the frequency range from 100 mHz to 100 kHz.

Electrosorptive capacity measurement

Graphite papers were used as inert current collectors on the back sides of the electrodes and the working electrodes of RGO-MF were prepared in the same manner as above in electrochemical measurements. The size of the electrode was 50 × 50 mm and each electrode mass was 0.1 g. A flow channel was created by punching a 1 cm diameter hole in the graphite sheet so that the solution could be in contact with all sides of the working electrodes and could run through the spacer to the outer reservoir. The electrosorptive capacity of the graphene-based electrode was conducted in a recirculating system including an electrosorptive unit cell and conductivity monitor as shown in Scheme S1 and Fig. 1.[43] The system was consisted of a reservoir, a peristaltic pump (BT-100), the CDI device, and a conductivity meter. A given potential was applied to the CDI cell using a potentiostat (RS1302DQ). The conductivity of the effluent water was measured by connecting a conductivity meter (DDS 307) at the position where the solution exited the cell. The CDI tests were conducted at potentials of 1, 1.2, 1.4, 1.8 or 2 V to compare the salt-removal efficiency at these values. NaCl solution with an initial conductivity in a total volume of 100 mL was continuously pumped into the unit cell by a peristaltic pump with a flow rate of 25 mL/min to the feed tank. The relationship between conductivity and concentration of NaCl solution can be found in Fig. S2. Herein, the electrosorptive capacity (q_e, mg/g) of current electrodes is calculated according to the following equations:[44]

$$q_e = \frac{(C_0 - C_e)V}{m} \quad (2)$$

Where C_0 (mg/mL) and C_e (mg/mL) are the initial and equilibrated NaCl concentrations, respectively; V (mL) is the volume of the container and m (g) is the mass of active components in two working electrodes.

Characterization

The morphology of MF nanoparticles and RGO-MF composites were examined by scanning electron microscopy (SEM, Zeiss EVO18) operating at 10 KV, and all samples were sputter-coated with a thin overlayer of gold to prevent sample charging effects. They were also observed by transmission electron microscopy (TEM, JEOL JEM-100CX II) at an accelerating voltage of 200 kV, powdered samples were dispersed in ethanol by ultrasonication for 10 min. The zeta potential of GO and MF nanoparticles were measured using a Zetasizer Nano ZS90 instrument (Malvern, UK). Thermal gravity analysis (TGA) was performed using a NETZSCH TG 209F3 instrument under a nitrogen atmosphere and a heating rate of 10 ^{o}C/min from 30 to 700 ^{o}C. The X-ray diffraction (XRD) pattern of MF nanoparticles and RGO-MF composites were obtained using an X'pert PRO diffractometer (40 kV and 40 mA) equipped with a Cu Kα radiation (wavelength 0.154 nm) at room temperature. Theta Probe X-ray Photoelectron Spectroscopy (XPS, ESCA Axis Ultra DLD) was used to verify the valence state of carbon and nitrogen. The Brunauer-Emmett-Teller (BET) method was

utilized to calculate the specific surface area. The pore size distributions were derived from desorption branch by using the Barrett-Joyner-Halenda (BJH) model. Before the measurements, all samples were degassed overnight at 493 K in a vacuum line. Photographs of vials containing suspension were taken with a Canon digital camera (IXUS 9515).

Results and discussion

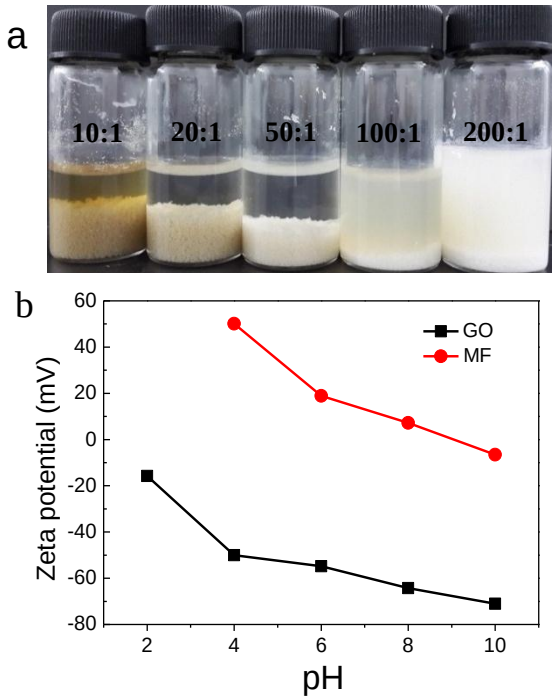

Fig. 2 (a) Photographs of the vessels containing complexes of GO and MF with different mass ratio of MF to GO from 10:1 to 200:1. The MF concentration was kept at the constant of 5 mg/mL and the pH value was 4. (b) Zeta potentials of GO sheets and MF nanoparticle at different pH values.

3D porous graphene network have been prepared by several approaches, such as hydrothermal treatment and chemical reduction.[45, 46] Herein, we present a simple and effective route to fabricate the polymer composites with 3D interconnected graphene networks by using a self-assembly and sintering process.[47] Compared with solvent processing method or vacuum filtration, the resulting 3D graphene network fabricated by our approach can realize a uniform distribution of GO sheets without aggregation in polymer matrix and separated by large pores created by MF particles. Additionally, under the optimal assembly conditions, the aqueous solution was transparent, indicating almost all the spheres were encapsulated and connected by GO in the complexes. Fig. 2a is the photographs of vessels containing precipitations of MF nanoparticles and GO sheets. From left to right, the mass ratio of MF nanoparticles to GO sheets ϕ are 10:1, 20:1, 50:1, 100:1 and 200:1, respectively. We can find that when ϕ=10:1, only partial GO could be assembled with MF spheres, leaving a yellow GO suspension. It meant that excessive GO sheets were dispersing in water rather than wrapping MF nanoparticles. While ϕ increased to 20:1, the aqueous solution was almost transparent and totally clear when ϕ=50:1. The supernatant began to be turbid if ϕ exceeded 100:1.

It should be noted that pH has an important effect on the electrostatic interactions between GO and MF. The pH values of all MF suspension and GO suspension were 4 because the spontaneous aggregates immediately formed once these two dispersions contacted at pH value of 4. As shown in Fig. 2b, the zeta potential of GO sheets was all negative no matter in acidic (pH=2, 4, 6) or in alkaline (pH=8, 10) solutions due to the ionization of the oxygen-containing functional groups on basal planes of the carbon networks. Owing to the acid soluble phenomenon of MF nanoparticle in solution of pH=2,[48] we choose the pH values of MF dispersions from 4 to 10. Its surface charges switched from positive (zeta potential, 50 mV) to negative (zeta potential, -7 mV) with increasing pH value from 4 to 10. We can find that the biggest difference in zeta potential between GO and MF occurred under pH value of 4. Therefore, the optimal assembly conditions we chose were ϕ=20:1 and pH=4.

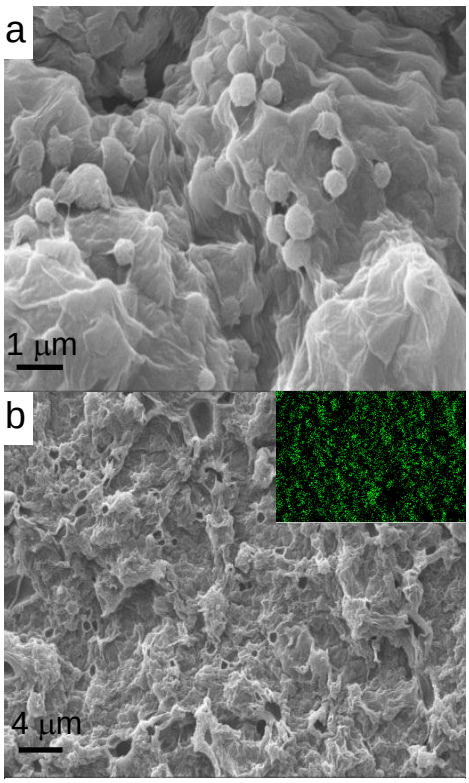

Fig. 3 SEM images of GO-MF-20 composites (a) before and (b) after sintering (RGO-MF-20). The inset in (b) is the corresponding EDS mapping of the N element.

The morphology and structure of GO-MF and RGO-MF composites were observed by SEM and TEM. From SEM image of GO-MF-20 in Fig. 3a, MF nanoparticles were uniformly distributed in the gap between GO sheets. Different from GO sheets without MF obtained from GO solution (Fig. S3), GO sheets encapsulated MF particles exhibited crinkled

and rough textures. No naked MF particles appeared in the SEM image and the edges of GO sheets were overlapped or linked between the adjacent particles to form a GO-MF framework in the coagulations. Under the effect of carbonization, the 3D macroporous graphene network of RGO-MF-20 was generated by the removal of MF particles, and GO was also thermally reduced simultaneously to RGO. As shown in Fig. 3b, a lot of pores were among graphene network and unique macroporous structure throughout the entire sample are preserved after the removal of MF templates. Meanwhile, gaseous products were vented when the MF nanoparticles were pyrolyzed under high temperature, which accelerated the sufficient exfoliation of 3D graphene network, leading to tremendous open porous channels in the 3D RGO-MF network. As shown in Fig. S4a, b, both concave pores and bulgy cavities were left after the carbonization of MF nanoparticles. The walls of 3D RGO-MF network consisted of flexible and wrinkled graphene sheets with a few layers, as observed in the high magnification TEM images in Fig. S4c, d. The inset in Fig. 3b is the corresponding EDS mapping of the N element. The nitrogen element was uniformly distributed in the RGO-MF composite, providing evidence for the successful nitrogen doping.

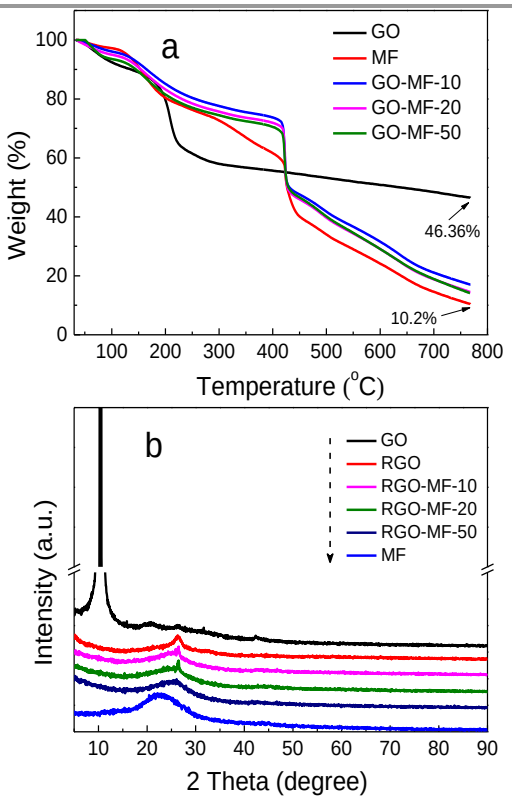

Fig. 4 (a) TG curves of GO, MF and GO-MF composites. (b) XRD patterns of GO, RGO, MF and RGO-MF composites.

The residual weight of N-rich MF nanoparticles was 10.2 % due to the unique chemical structure, as shown in the analysis of Fig. 4a, which was different from RGO-polystyrene (PS) composites prepared from PS nanoparticle templates with a complete pyrolysis.[49] GO nanosheets started to decompose at about 100 °C because of the adsorbed water, while the second weight loss was due to the decomposition of oxygen-containing functional groups, suggesting GO could be derived into graphene through the thermal reduction. The TG curves of GO-MF composites had similar stages to both GO and MF, but the residual weights were in the middle of GO and MF. Additionally, the weight loss stages at 422 °C of three composites are the same as MF nanoparticles, which also confirmed that MF nanoparticles were uniformly distributed in the gap between the GO sheets.

The XRD technique is widely employed to evaluate the interlayer distance and the exfoliation degree of graphene. As depicted in Fig. 4b, GO sheets exhibited a strong intense (001) peak at 2θ=10.3° and MF showed an intense peak at 22.5°. Compared with GO, the (001) peak at 10.3° disappeared and only a weak (002) peak at 2θ=26° appeared in the XRD patterns of 3D RGO-MF composites, indicating that most of the oxygen-containing groups on basal planes of the carbon networks had been removed.[50] More detailed information of (002) peaks can be found in Fig. S5. We can find that the 3D RGO-MF composite shows a similar XRD pattern to the pristine RGO, but the (002) peak becomes broader with the increase amount of MF nanoparticles in GO-MF composites. It meant that the introduction of MF nanoparticles had no significant effect on the macroporous network of 3D RGO-MF composites and promoted the exfoliation of graphene sheets.

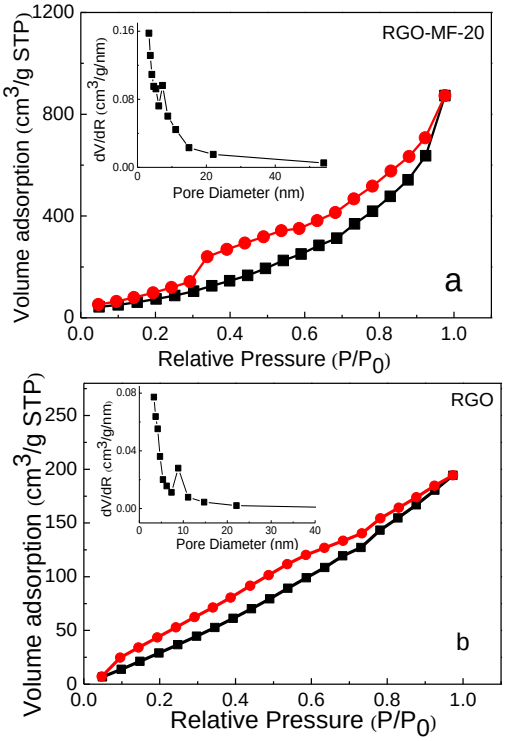

Fig. 5 Nitrogen sorption isotherms and pore size distribution (inset) of (a) RGO-MF-20 and (b) RGO.

The porous nature of all of the samples was further investigated by a nitrogen adsorption-desorption measurement. The specific surface areas (SSA), total pore volumes, average pore diameter of all electrodes are listed in Table S1. Among all samples, the specific surface area of RGO-MF-10, RGO-MF-20 and RGO-MF-50 is 292, 353.8 and 297 m^2/g, respectively, which is much larger than that of RGO (SSA=120 m^2/g). The higher surface area further confirms that the incorporation of MF nanoparticles effectively prevents the aggregation of individual graphene sheets during reduction. As shown in Fig. 5, the adsorption gradually increases in the region of middle P/P_0 and further in the region of high pressure >0.8 P/P_0. It can be concluded that this sample contains macropores together with the mesopores, in which macropores are resulting from the removal of MF nanoparticles and mesopores are attributed to the gas release through the high-temperature calcination process. In generally, the surface areas increased with the increase amount of MF in GO-MF composites. However, the surface area of RGO-MF-50 is smaller than that of RGO-MF-20, probably because the amount of MF nanoparticles have been saturated when the mass ratio of 50, which was in good accordance of Fig. 2a. Therefore, we choose RGO-MF-20 as the working electrode in CDI device.

In order to further prove the successful nitrogen doping into the graphene sheet frameworks, XPS is used to analyze the surface composition and chemical configuration of carbon and nitrogen atoms in all samples. Obviously in Fig. 6a, there are no N1s peaks in GO and RGO, and the XPS spectrum shows only the presence of carbon and oxygen atoms. Compared with GO, the intensities of all the peaks of oxygen functional groups in RGO-MF-20 are decreased dramatically and the intensity of the Csp^2 peak is increased simultaneously (Fig. 6b and 6c). Similar phenomenon can be found in Fig. S6a, the high-resolution C1s XPS spectrum of the RGO. This reveals that most of the oxygen groups have been removed, and the graphitic carbon network was partially restored, which is also confirmed by the FT-IR observation (Fig. S7). Similarly, the bonding configurations of nitrogen atoms in RGO-MF composites were characterized by high-resolution N1s spectra. XPS spectra for 3D RGO-MF composites clearly show the calculated N/C atomic ratio of RGO-MF-10, 20, 50 is 4.6, 12.8 and 18.5% by controlling the introduced amount of MF nanoparticles in GO-MF composites, as shown in Table S2. It indicates that N-doping level of 3D RGO-MF composites will increase with the increase of melamine mass.[51] The peaks with lower binding energy located at about 398.2 and 399.7 eV, correspond to pyridine-like (C=N-C) and pyrrole-like ($N-(C)_3$) nitrogen, which can contribute to the π-conjugated system with a pair of p-electrons in the graphene layers. When carbon atoms within the graphene layers are substituted by nitrogen atoms in the form of "graphitic" nitrogen, the peak with the highest binding energy at 401.3 eV corresponds to the quaternary nitrogen.[52] No matter in our prepared 3D RGO-MF composites or MF, pyridine-like nitrogen is the main component (Table S3). However, the proportion of quaternary nitrogen located within the graphene sheets of 3D RGO-MF composites are much bigger than pure MF sample, while the amount of peripheral pyridine nitrogen decreases. These results indicate that the pyridine nitrogen has been chemically transformed into nitrogen species with higher binding energies through the condensation reactions occurring during carbonization.[53] Compared RGO-MF-10 and RGO-MF-50, the proportion of quaternary nitrogen of RGO-MF-20 are a little bigger than others, which again confirms that RGO-MF-20 is most appropriate as the working electrode in CDI device.

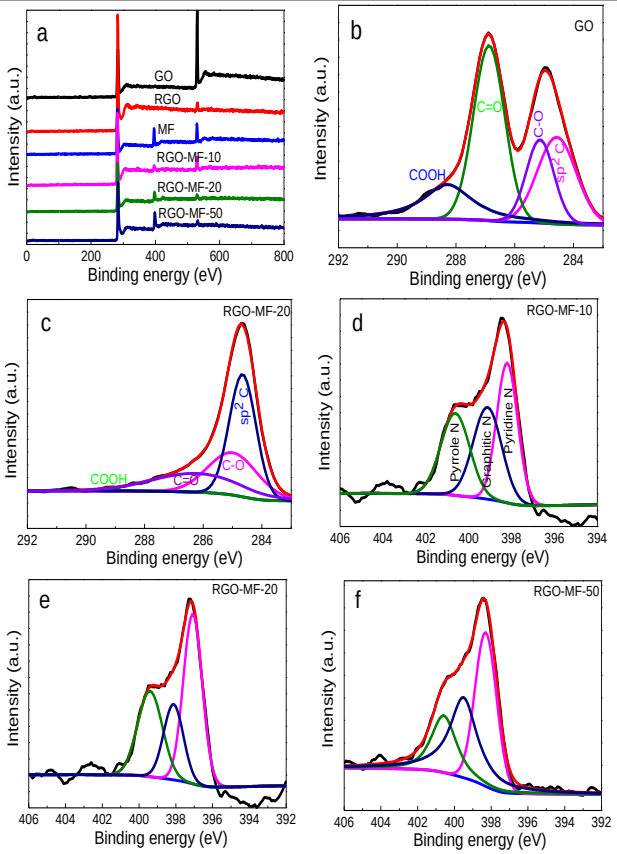

Fig. 6 (a) Survey scans of the XPS spectra. XPS C1s core level spectra of (b) GO and (c) RGO-MF-20. XPS N1s core level spectra of (d) RGO-MF-10, (e) RGO-MF-20, and (f) RGO-MF-50.

Electrochemical performance

In order to analyze the electrochemical properties of the prepared electrodes, CV measurements were used to evaluate the electrosorption ability of 3D RGO-MF composites. CV analysis of as-prepared graphene electrodes are depicted in Fig. 7. The CV profiles of the 3D RGO-MF and pristine RGO electrodes in a 0.5 M NaCl aqueous solution with a potential of -1 to 0 V are displayed in Fig. 7a. As clearly seen, no obvious Faradaic reaction is observed in the CV curves, which suggests that the CV behavior results from the electric double layer capacitance (EDLC) due to the Coulombic interactions and most of the oxygen-containing groups are removed.[54] We can find that the CV curves of 3D RGO-MF electrode deviate from rectangular shape due to N-doping, comparing with pure RGO

electrode. However, the symmetrical curves of both electrodes indicate that the capacitive process is a highly stable process and imply excellent electrochemical double-layer capacitance have been developed at a comparable rate during the electro process. Furthermore, when the scanning rate increased from

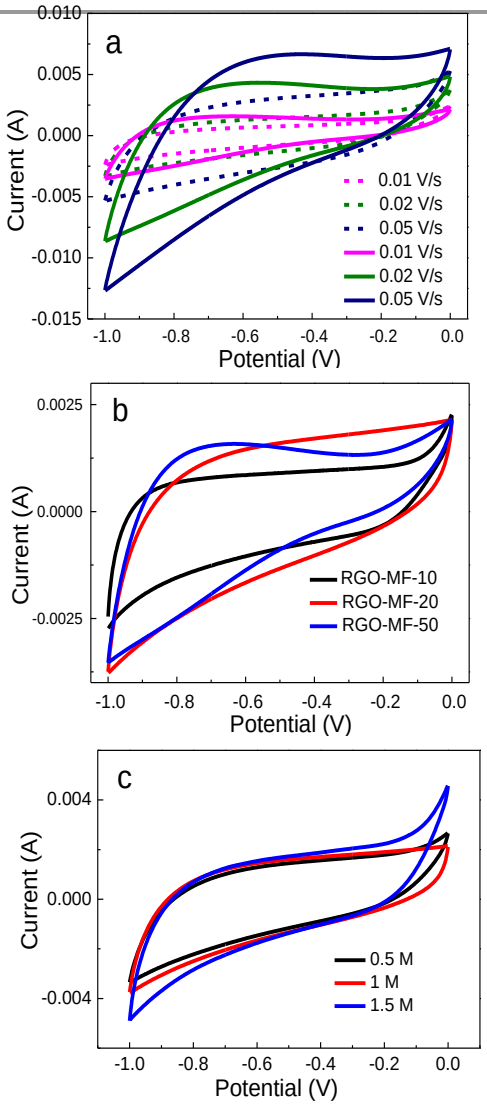

Fig. 7 (a) Comparative CV curves of RGO-MF-20 and RGO electrodes at various scan rates (solid line: RGO-MF-20 and dash line: RGO). (b) CV curves of RGO-MF-10, 20 and 50 electrodes at a scan rate of 10 mV/s. The curves in (a) and (b) were obtained in a 0.5 M NaCl aqueous solution. (c) Comparative CV curves of RGO-MF-20 electrode at various NaCl concentrations.

0.01 to 0.05 V/s, the current response of the 3D RGO-MF composite electrode is always higher than that of the RGO electrode at any chosen scanning rate. So the 3D RGO-MF composites contribute to an increase in the capacitance and are more desirable for fabricating the 3D porous electrode for CDI application. The higher specific capacitance of the 3D RGO-MF electrode can be ascribed to the improved specific surface area and hierarchical pore structure prepared by the introduction of MF nanoparticles. Firstly, the 3D macroporous structures minimize the ion diffusion distances to the interior surfaces, so the effective and fast ion diffusion is realized during the electrochemical procedure. Secondly, mesoporous produced by the release of gases provide low-resistant pathways for the ions through into the deep region of the 3D structure. Additionally, the lone electron pairs of nitrogen atoms can form a delocalized conjugated system with the sp^2-hybridized carbon frameworks, so the electronegativity of nitrogen is stronger than that of carbon, which results in great improvement of the reversible capacity of 3D RGO-MF electrodes. As is well known, the higher specific capacitance of the electrode in the CV measurement means that the higher deionization efficiency would be obtained, because more salty ions could be removed under certain direct voltage during the CDI process. Therefore, the 3D RGO-MF electrode shows great superiority for CDI application.

Fig. 7b shows the CV curves of sample RGO-MF-10, -20 and -50 electrodes at a scan rate of 0.01 V/s. The CV curves deviate more from rectangular shape with the increased amount of MF nanoparticles. The scan rate was slow enough to eliminate kinetic effects during the sorption of ions. This deviation was related to the pseudocapacitive properties of the present samples. It should be suggested due to the introduction of nitrogen in an appreciable amount. We know that the pyridinic nitrogen is located at the easily accessible edges of graphene layers, and therefore they can easily contribute to the total capacitance with the pseudocapacitive effect. Therefore more salty ions can be adsorbed on the surface of the 3D RGO-MF electrodes through 3D interconnected hierarchy pores because of more N-doping. To further investigate the electrosorption capacity of the 3D RGO-MF electrode, we have changed the concentration of aqueous electrolyte. Fig. 7c is the CV curves of RGO-MF-20 in NaCl aqueous solutions with different concentrations (0.5-1.5 M). But overall no significant differences can be seen among three CV curves, indicating that 3D RGO-MF electrodes have electrochemically stable behavior and excellent electrochemical double-layer capacitance during the electro adsorption/desorption process.

GC measurements were carried out to further investigate the electrosorption performance of the 3D RGO-MF and RGO electrodes at the current density of 0.3 A/g in a 0.5 M NaCl solution, with a potential window of -1 to 0 V (Fig. 8a). As shown in Fig. 8a, the GC curves of both the 3D RGO-MF and RGO electrodes display analogous triangular shapes during the charge-discharge process, indicating that the electrodes exhibit a good reversibility. But the CV curves of 3D RGO-MF electrode deviate more from triangular shape due to N-doping, which is in good agreement with the above CV measurements. According to the calculating equation 1, the Cs of 3D RGO-MF electrode is much larger than that of RGO electrode because the discharge time of the RGO-MF-20 electrode is obvious longer than that of the RGO one. In fact, the gravimetric capacitance of RGO (23.3 F/g) is almost 3 times less than that of RGO-MF-20 (76.8 F/g) in 0.5M NaCl solution. The enhanced capacity results from the 3D interconnected conductive networks and abundant N-doping. Compared with the RGO-MF electrodes, the Cs of pure RGO electrodes prepared without nitrogen nanoparticles is much smaller (58.4 F/g).[49] For the investigation

of the cycle performance, the continuous GC measurement of the 3D RGO-MF electrode was conducted in a 0.5 M NaCl aqueous solution. **Fig.** 8b shows the continuous GC curves of

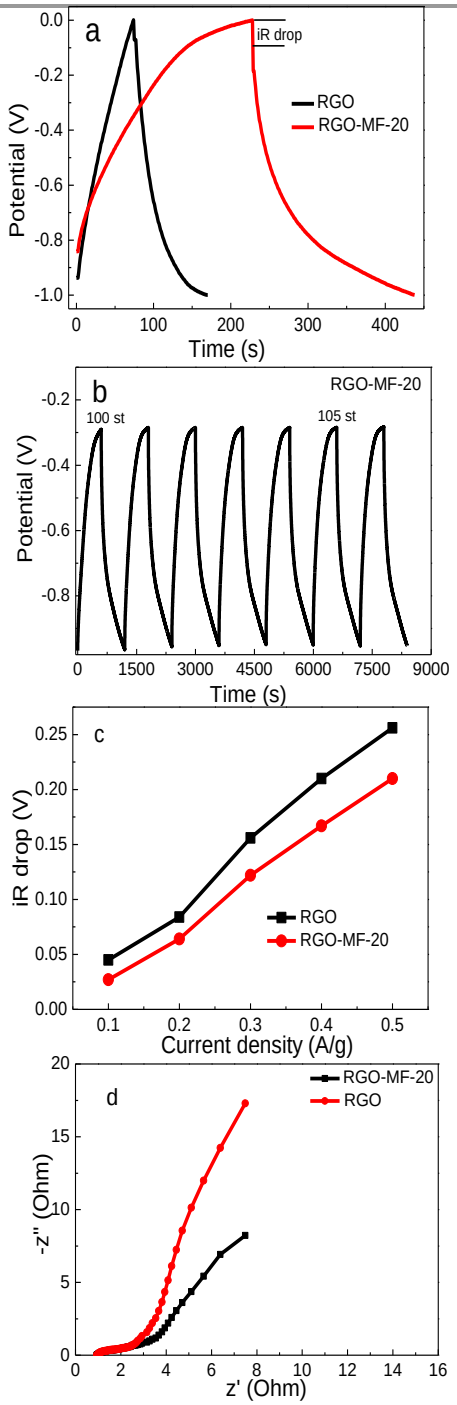

Fig. 8 (a) Galvanostatic charge (GC) curves of RGO-MF-20 and RGO electrodes with a current density of 0.3 A/g. (b) Continuous GC curves of the RGO-MF-20 electrode with a current density of 0.3 A/g. (c) The variation tendency of the iR drop against the current density of the 3D RGO-MF-20 and RGO electrodes and (d) Nyquist plots of the EIS for the RGO and RGO-MF-20 electrodes.

the RGO-MF-20 electrode with a current density of 0.3 A/g. Clearly, the charge–discharge curves exhibit nearly linear potential-time plots in the whole potential range, demonstrating that the 3D RGO-MF electrode exhibits good stability in repeat charge–discharge processes. For the comparison, continuous GC curves of the RGO electrode are shown in Fig. S8. Obviously, RGO-MF-20 electrode exhibits higher capacitance than the pristine RGO during the entire cycle. Therefore, the 3D RGO-MF electrode with a better cyclability and stability would have a better CDI performance. As shown above, all the curves display triangular shapes with a low potential drop (iR drop) at the beginning of the discharge processes, which is caused by the entire inner resistance of the electrode. Furthermore, the iR drop value is much lower at a relatively lower current density and increases with the increasing discharge current density, as shown in Fig. 8c. Additionally, 3D RGO-MF electrode possesses a much lower iR drop than the pristine RGO, which indicates a significantly reduced inner resistance, due to the sufficient exfoliation and reduction of graphene sheets in the walls of RGO-MF composites. Fig. 8d shows the resulting Nyquist plots of the EIS spectra for the RGO and RGO-MF-20 electrodes. The intercept of the semicircle on the real axis at high frequency represents the equivalent series resistance (Rs), and the diameter of the semicircle corresponds to the charge-transfer resistance (Rct) of the electrode. As shown in Fig. 8d, the diameter of both semicircles is very small, suggesting a negligible interfacial electron-transfer resistance. Additionally, the Rs of RGO-MF-20 electrodes are approximate ~1.0 Ω, which ensures a faster charge/discharge rate and a highly efficient electrosorption behaviour. It is noteworthy that, the slope of straight line of RGO-MF-20 at low frequency is obvious smaller than that of RGO, indicating good capacitive property and easy diffusion of the salt ions onto the electrode surface.

CDI performance

The desalination behaviors and regeneration performances of the 3D RGO-MF and RGO electrodes were measured by batch mode experiments with similar conditions. As is well known, the voltage has a significant effect on the total capacity, especially at high voltages. So the CDI performances of 3D RGO-MF electrodes under different voltages ranging from 1.0 to 2.0 V with an initial conductivity of 300 μS/cm were investigated.[55] Fig. **9**a shows the deionization curves at five different applied voltages: 1.0, 1.2, 1.6, 1.8, and 2.0 V. With the voltage increased from 1.0 to 2.0 V, the electrosorptive capacity gradually increased from 0 to 23.18 mg/g. As expected, the high voltage results in a high electrosorptive capacity because of the electrostatic force. It is noteworthy that when the applied voltage is 1.0 V, the conductivity doesn't decrease with time. It should be due to the release of the residual salts in electrodes during the process of fabrication and 1.0 V is not big enough to absorb NaCl from the solution. Furthermore, when the applied voltage was higher than 1.4 V, the conductivity obviously decreases with time, indicating that the higher voltage leads to a higher electrosorptive capacity because of the stronger Coulombic interaction. However, even when the applied voltage is at 2.0 V, no visible gas bubbles were observed, indicating that no water electrolysis was taking place.[56] Therefore, all CDI tests herein were carried under 2.0 V.[57]

Journal Name RSCPublishing

ARTICLE

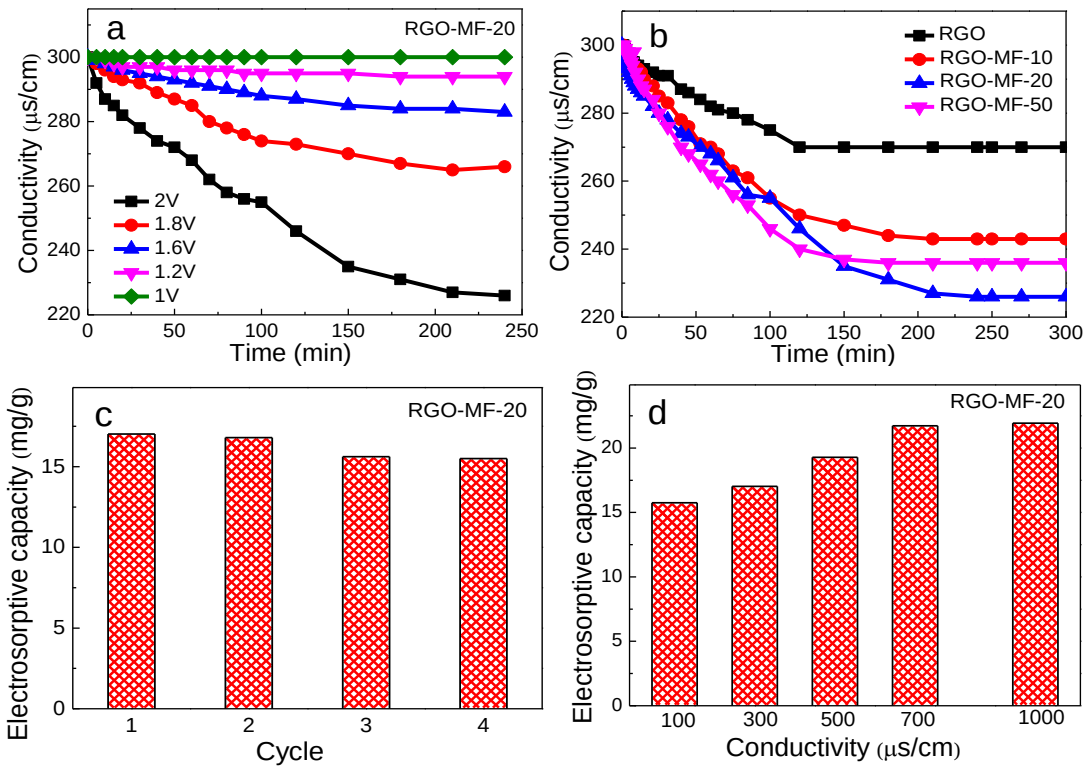

Fig. 9 (a) CDI profiles of RGO-MF-20 electrode under various voltages, (b) CDI profiles of the RGO and RGO-MF-10, 20, 50 electrodes under 2.0 V, (c) Regenerated electrosorptive capacity of RGO-MF-20 electrode, (d) The electrosorption capacity of 3D RGO-MF-20 electrode in NaCl solutions with different initial concentrations.

Fig. 9b shows the CDI profiles of the RGO and RGO-MF-10, 20, 50 electrodes under 2.0 V with an initial conductivity of 300 μS/cm. As we can see, the conductivity of all electrodes decreased at the initial stage, which demonstrated the adsorption of salt ions by oppositely charged carbon electrode. As the time went on, the conductivity decreased continuously, but the rate began to slow down until adsorption equilibrium was reached. Finally, the conductivity tended to be stable, suggesting the electrosorption of these electrodes was saturated, because the electrostatic repulsion between the adsorbed ions prevents the constancy of electrosorption. In contrast, the conductivity change of RGO electrode is much smaller than 3D RGO-MF electrodes under the same experiment conditions, indicating a faster ion removal behavior of the 3D RGO-MF electrode. According to Equation 2, the electrosorptive capacities were 13.02, 17.02, 14.72, and 6.89 mg/g for the RGO-MF-10, -20, -50 and pristine RGO electrodes, respectively. The enhanced salt removal performance can be attributed to the numerous adsorption pores resulting from the 3D hierarchy architecture of the 3D RGO-MF electrode. Apart from the high specific capacitance and excellent electrical conductivity, the reversibility and stability of the carbon electrode are also regarded as important factors for a high performance CDI application. After the electrodes reach their adsorption capacity (which depends on cell voltage), a discharge cycle is initiated by reducing or reversing the cell voltage, thereby releasing the salt as a concentrated stream. In addition, the electrosorptive capacity of RGO-MF-20 was 17.02 mg/g, much higher as compared with those reported by other literatures.[30,31] On the one hand, the weight (*m*) of each active electrode in this work was 0.1 g, much smaller than those in other literatures. Hence the thickness of the electrode was thinner, which further facilitated electrolyte diffusion and transport into the RGO-MF composite. The efficiency of RGO-MF electrodes for absorbing NaCl would be also improved before porous holes were saturated with the ionic species. On the other hand, the enhanced capacity resulted from the 3D interconnected conductive networks and abundant N-doping also greatly increased the electrosorptive capacity of RGO-MF-

20 electrode. As a result, the electrosorptive capacity in this work is finely high.

Fig. 9c shows the regenerated electrosorptive capacity of one RGO-MF-20 electrode, and the electrosorptive capacities are 17.02, 16.53, 15.62, 15.51 mg/g from the first to forth time. As we expected, ions can be removed in the adsorption process and released in the desorption process with no noticeable decrease in the initial conductivity in all four consecutive cycles, confirming that the CDI could be regenerated very well without any driving energy and secondary pollution which is critical for large scale application. Furthermore, the adsorbed ions can effectively return back to the bulk solution with the absence of an external potential, so the electrode can be regenerated for further use without any secondary waste. The regeneration cycles of the RGO and RGO-MF-20 electrodes with the absence of an external potential can be found in Fig. S9. As shown in Fig. 9d, the total capacity increases as the ion solution concentration is increased. The electrosorptive capacities are 15.75, 17.02, 19.28, 21.73, 21.93 mg/g as the initial concentrations of the NaCl solutions are 100, 300, 500, 700, 1000 μs/cm. In fact, the electrical double layer thickness is inversely proportional to the solution concentration. Specially, with a lower concentration, the electric field can extend to a longer distance since the solution is less effective in holding the charge.[58] However, the concentration has a significant effect on the total capacity only at low concentrations. When the concentration exceeds a certain value, the porous holes are saturated with the ionic species and any further increase of the concentration does not increase the total capacity.

Conclusions

A novel 3D RGO-MF composite were prepared by the incorporation of MF nanoparticles within the graphene sheets. After filtration and carbonization, the as-prepared RGO-MF composites showed a porous 3D interconnected network structure and high electrical conductivity due to the strong electrostatic interactions between GO and MF. Under the optimal mass ratio of MF to GO, RGO-MF-20 composites demonstrate largest specific surface area and highest quaternary nitrogen proportion. Therefore, RGO-MF-20 was fabricated as the electrode for electrochemical test and application in capacitive removal of salty ions. Prominent CV measurements demonstrated that the RGO-MF-20 had a high specific capacitance of 76.8 F/g, which was much larger than the RGO electrode and no-nitrogen doping graphene electrodes. Further GC tests confirmed that the electrodes exhibit a good reversibility, and lower iR drop meant lower inner resistance of 3D RGO-MF composites. The enhanced electrochemical properties of the 3D RGO-MF electrodes lead to an outstanding specific electrosorptive capacity of 21.93 mg/g. In conclusion, the 3D RGO-MF composites are well suited as a high performance CDI electrode material and can be further investigated on promising electrode material for cost effective, energy-optimised CDI technology.

Acknowledgements

This work was financially supported by the National Natural Basic Research Program of China (973 Program, 2012CB821500), the National Natural Science Foundation of China (21274046 and 21474032) and the Natural Science Foundation of Guangdong Province (S2012020011057).

Notes and references

Research Institute of Materials Science, South China University of Technology, Guangzhou 510640, China. Fax: +86-20-22236269; Tel: +86-20-22236269; E-mail: zhywang@scut.edu.cn

† Electronic Supplementary Information (ESI) available: SEM and TEM images of RGO, MF nanoparticles and 3D RGO-MF-20 composite, XRD patterns of RGO and RGO-MF composites, FTIR spectra of GO, MF and RGO-MF-20 composite, N_2 adsorption/desorption isotherms of RGO and RGO-MF composites, XPS spectra of RGO and RGO-MF composite, and GC curves of the RGO electrode. See DOI: 10.1039/b000000x/.

1. I. C. Karagiannis and P. G. Soldatos, *Desalination*, 2008, **223**, 448.
2. S. Raphael, *Environ. Sci. Technol.*, 2008, **42**, 8193.
3. M. A. Anderson, A. L. Cudero and J. Palma, *Electrochim. Acta*, 2010, **55**, 3845.
4. C. Tsouris, R. Mayes, J. Kiggans, K. Sharma, S. Yiacoumi, D. DePaoli and S. Dai, *Environ. Sci. Technol.*, 2011, **45**, 10243.
5. Y. A. C. Jande and W. S. Kim, *Desalination*, 2013, **329**, 29.
6. L. Han, K. G. Karthikeyan, M. A. Anderson, J. J. Wouters and K. B. Gregory, *Electrochim. Acta*, 2013, **90**, 573.
7. J. Chmiola, G. Yushin, Y. Gogotsi, C. Portet, P. Simon and P. L. Taberna, *Science*, 2006, **313**, 1760.
8. D. W. Wang, F. Li, M. Liu, G. Q. Lu and H. M. Cheng, *Angew. Chem. Int. Ed.*, 2008, **47**, 373.
9. S. Porada, L. Borchardt, M. Oschatz, M. Bryjak, J. S. Atchison, K. J. Keesman, S. Kaskel, P. M. Biesheuvel and V. Presser, *Energ. Environ. Sci.*, 2013, **6**, 3700.
10. S. Porada, L. Weinstein, R. Dash, A. van der Wal, M. Bryjak, Y. Gogotsi and P. M. Biesheuvel, *ACS Appl. Mater. Inter.*, 2012, **4**, 1194.
11. M. Haro, G. Rasines, C. Macias and C. O. Ania, *Carbon*, 2011, **49**, 3723.
12. P. Xu, J. E. Drewes, D. Heil and G. Wang, *Water Res.*, 2008, **42**, 2605.
13. T. Y. Ma, L. Liu and Z. Y. Yuan, *Chem. Soc. Rev.*, 2013, **42**, 3977.
14. M. Oschatz, L. Borchardt, M. Thommes, K. A. Cychosz, Y. Gogotsi and S. Kaskel, *Angew. Chem. Int. Ed.*, 2012, **51**, 7577.
15. L. X. Li, L. Zou, H. H. Song and G. Morris, *Carbon*, 2009, **47**, 775.
16. H. B. Li, Y. Gao, L. K. Pan, Y. P. Zhang, Y. W. Chen and Z. Sun, *Water Res.*, 2008, **42**, 4923.
17. L. Estevez, R. Dua, N. Bhandari, A. Ramanujapuram, P. Wang and E. P. Giannelis, *Energ. Environ. Sci.*, 2013, **6**, 1785.
18. Z. Y. Lin, Z. Li, K. S. Moon, Y. N. Fang, Y. G. Yao, L. Y. Li and C. P. Wong, *Carbon*, 2013, **63**, 547.
19. Z. Peng, D. S. Zhang, T. T. Yan, J. P. Zhang and L. Y. Shi, *Applied Surface Science*, 2013, **282**, 965.
20. K. B. Hatzell, L. Fan, M. Beidaghi, M. Boota, E. Pomerantseva, E. C. Kumbur and Y. Gogotsi, *ACS Appl Mater Interfaces*, 2014, **6**, 8886.
21. Z. Peng, D. S. Zhang, L. Y. Shi and T. T. Yan, *J. Mater. Chem.*, 2012, **22**, 6603.
22. P. Kumar, *RSC Adv.*, 2013, **3**, 11987.
23. Z. H. Ni, T. Yu, Y. H. Lu, Y. Y. Wang, Y. P. Feng and Z. X. Shen, *ACS nano*, 2008, **2**, 2301.
24. H. Bi, S. R. Sun, F. Q. Huang, X. M. Xie and M. H. Jiang, *J. Mater. Chem.*, 2012, **22**, 411.
25. C. W. Lo, D. F. Zhu and H. R. Jiang, *Soft Matter*, 2011, **7**, 5604.
26. W. Lv, C. H. You, S. D. Wu, B. H. Li, Z. P. Zhu, M. Z. Wang, Q. H. Yang and F. Y. Kang, *Carbon*, 2012, **50**, 3233.
27. P. Simon and Y. Gogotsi, *Accounts. Chem. Res.*, 2012, **46**, 1094.

28. H. Wang, L. Y. Shi, T. T. Yan, J. P. Zhang, Q. D. Zhong and D. S. Zhang, *J. Mater. Chem. A*, 2014, **2**, 4739.
29. D. S. Zhang, X. R. Wen, L. Y. Shi, T. T. Yan and J. P. Zhang, *Nanoscale*, 2012, **4**, 5440.
30. X. R. Wen, D. S. Zhang, T. T. Yan, J. P. Zhang and L. Y. Shi, *J. Mater. Chem. A*, 2013, **1**, 12334.
31. D. S. Zhang, T. T. Yan, L. Y. Shi, Z. Peng, X. R. Wen and J. P. Zhang, *J. Mater. Chem.*, 2012, **22**, 14696.
32. G. X. Luo, L. Z. Liu, J. F. Zhang, G. B. Li, B. L. Wang and J. J. Zhao, *ACS Appl. Mater. Inter.*, 2013, **5**, 11184.
33. G. Wei, Y. E. Miao, C. Zhang, Z. Yang, Z. Y. Liu, W. W. Tjiu and T. X. Liu, *ACS Appl. Mater. Inter.*, 2013, **5**, 7584.
34. Y. Yang, Y. H. Deng, Z. Tong and C. Y. Wang, *J. Mater. Chem. A*, 2014, **2**, 9994.
35. S. M. Li, S. Y. Yang, Y. S. Wang, C. H. Lien, H. W. Tien, S. T. Hsiao, W. H. Liao, H. P. Tsai, C. L. Chang, C. C. M. Ma and C. C. Hu, *Carbon*, 2013, **59**, 418.
36. W. Fan, Y. Y. Xia, W. W. Tjiu, P. K. Pallathadka, C. B. He and T. X. Liu, *J. Power Sources*, 2013, **243**, 973.
37. K. H. Lee, J. Oh, J. G. Son, H. Kim and S. S. Lee, *ACS Appl. Mater. Inter.*, 2014, **6**, 6361.
38. Y. Yang, Z. Tong, T. Ngai and C. Y. Wang, *ACS Appl. Mater. Inter.*, 2014, **6**, 6351.
39. S. Q. Ye, C. Y. Wang, X. X. Liu, Z. Tong, B. Y. Ren and F. Zeng, *J. Control. Release*, 2006, **112**, 79.
40. Y. Yang, Y. Ning, C. Y. Wang and Z. Tong, *Polym. Chem.*, 2013, **4**, 5407.
41. W. S. Hummers and R. E. Offeman, *J. Am. Chem. Soc.*, 1958, **80**, 1339.
42. X. Y. Gu, Y. Ning, Y. Yang and C. Y. Wang, *RSC Adv.*, 2014, **4**, 3211.
43. Y. J. Kim and J. H. Choi, *Water Res.*, 2010, **44**, 990.
44. B. P. Jia and L. Zou, *Carbon*, 2012, **50**, 2315.
45. H. P. Cong, X. C. Ren, P. Wang and S. H. Yu, *ACS Nano*, 2012, **6**, 2693.
46. Y. Wimalasiri and L. Zou, *Carbon*, 2013, **59**, 464.
47. C. Wu, X. Y. Huang, G. L. Wang, L. B. Lv, G. Chen, G. Y. Li and P. K. Jiang, *Adv. Funct. Mater.*, 2013, **23**, 506.
48. P. Thomas, G. Markus and P. Johann, *J. Appl. Polym. Sci*, 2013, **127**, 3705.
49. H. Wang, D. S. Zhang, T. T. Yan, X. R. Wen, J. P. Zhang, L. Y. Shi and Q. D. Zhong, *J. Mater. Chem. A*, 2013, **1**, 11778.
50. L. Kou and C. Gao, *Nanoscale*, 2013, **5**, 4370.
51. Z. H. Sheng, L. Shao, J. J. Chen, W. J. Bao, F. B. Wang and X. H. Xia, *ACS Nano*, 2011, **5**, 4350.
52. N. Xiao, D. M. Lau, W. H. Shi, J. X. Zhu, X. C. Dong, H. H. Hng and Q. Y. Yan, *Carbon*, 2013, **57**, 184.
53. D. Hulicova, J. Yamashita, Y. Soneda, H. Hatori and M. Kodama, *Chem. Mater.*, 2005, **17**, 1241.
54. Z. Peng, D. S. Zhang, L. Y. Shi, T. T. Yan, S. Yuan, H. R. Li, R. H. Gao and J. H. Fang, *J. Phys. Chem. C*, 2011, **115**, 17068.
55. K. L. Yang, T. Y. Ying, S. Yiacoumi, C. Tsouris and E. S. Vittoratos, *Langmuir*, 2001, **17**, 1961.
56. H. B. Li, T. Lu, L. K. Pan, Y. P. Zhang and Z. Sun, *J. Mater. Chem.*, 2009, **19**, 6773.
57. H. B. Li, L. Zou, L. K. Pan and Z. Sun, *Environ. Sci. Technol.*, 2010, **44**, 8692.
58. H. B. Li, S. Liang, J. Li and L. J. He, *J. Mater. Chem. A*, 2013, **1**, 6335.